PCCP

Scaling and dynamics of "flow distributed oscillation patterns" in the Belousov–Zhabotinsky reaction

J. R. Bamforth,[ab] R. Tóth,[c] V. Gáspár[c] and S. K. Scott[a]

[a] *School of Chemistry, University of Leeds, Leeds, UK LS2 9JT*
[b] *Department of Chemical Engineering, University of Leeds, Leeds, UK LS2 9JT*
[c] *Institute of Physical Chemistry, University of Debrecen, 4010 Debrecen, P.O. Box 7, Hungary*

Received 22nd August 2001, Accepted 27th September 2001
First published as an Advance Article on the web 15th January 2002

The formation of "flow distributed oscillation" (FDO) patterns in the Belousov–Zhabotinsky (BZ) reaction is studied experimentally. We confirm the dependence of the pattern wavelength on the flow velocity and the concentration of the reactant species BrO_3^- and H^+ as predicted in a previous study. We also report on the initial development of the FDO patterns. In contrast to simple interpretations, the patterns arise through a "wave splitting" mechanism in which a pair of counter-propagating wave pulses are created from a pacemaker site at some distance ahead of the pattern: one of these waves propagates with the flow and leaves the reactor, the other propagates against the flow and eventually settles to form the next band of the FDO pattern. This initiation mechanism is confirmed in numerical studies based on the Oregonator model. These computations also indicate the possibility of complex dynamics similar to the "resonance patterns" reported in studies of the propagation of BZ waves through capillary tubes.

1. Introduction

The mechanism of stationary spatial pattern formation through "flow-distributed oscillations" was first proposed by Kuznetsov *et al.*[1] and developed in subsequent papers[2,3] using the Brusselator model. FDO patterns arise for a chemical reaction system capable of exhibiting long-lived oscillatory behaviour in a batch reactor. The spatial patterning arises when the reactants are fed first into a continuously-fed well-stirred reactor (CSTR) and from there into a plug-flow or packed-bed in which the reacting fluid flows with no longitudinal mixing. The CSTR is operated under steady-state conditions so that all fluid volume elements entering the plug-flow reactor have the same initial phase. A heuristic argument then indicates that the quotient of the distance along the plug-flow reactor and the flow velocity corresponds to reaction time and hence a fixed oscillatory period in time will be translated into a fixed wavelength along the tube. This argument does not predict an important feature, namely that there is a critical, minimum flow rate along the reactor below which the stationary patterns are not observed, but it does predict, at least for conditions well above the minimum flow rate, a linear relationship between the wavelength and the flow velocity. This linear dependence has been confirmed numerically with the Oregonator and other models, including the chlorine dioxide–iodine–malonic acid (CDIMA) reaction,[4] although Andresen *et al.*[3] also indicate a nonlinear response close to the critical flow rate using an extended model for the Belousov–Zhabotinsky (BZ) reaction. Kærn and Menzinger[5] provided the first experimental realisation of FDO patterns using the BZ reaction and observed a linear dependence of wavelength on flow rate, but they were unable to determine a critical flow-rate or any nonlinear behaviour.

In a recent paper,[6] we reported a theoretical and numerical analysis of FDO patterns in the Oregonator model of the BZ system. The main results were the identification of the critical conditions for the existence of such spatial structures and, hence, the regions of the experimental parameter domain (in terms of the concentrations of the pool chemical reactant species BrO_3^-, malonic acid (MA) and H^+) and the expected dependence of the wavelength of the FDO pattern on these concentrations. The critical flow velocity was shown to correspond typically to very low flow rates—perhaps inaccessible experimentally. The wavelength of fully-developed patterns was predicted to scale linearly with the flow rate ϕ_P and as the inverse square root of the bromate and H^+ concentrations:

$$\lambda \sim \frac{\phi_P}{[BrO_3^-]^{1/2}[H^+]^{1/2}}$$

In this paper, we describe an experimental test of these predictions. Additionally, we address the question of the transient dynamics leading to the development of the ultimately time-independent pattern from an initially spatially-uniform state. This latter point is also investigated numerically.

2. Experimental

2.1 Chemicals

Malonic acid (Fisher, 99%), potassium bromate (Fisher, 99%) and sulfuric acid (Fisher, 98%) were used without further purification. Ferroin, $Fe(phen)_3^{2+}$, was prepared by dissolving $FeSO_4$ and 1,10-phenanthroline in a 1 : 3 ratio in acidic solution and then filtering the solution to remove any undissolved solids.[7] All reagent solutions were prepared freshly in doubly-distilled de-ionised water before each set of experiments.

2.2 Apparatus and procedure

The apparatus comprised a CSTR of volume 6.5 ml stirred by a magnetic impeller and supplied from stock solutions containing (a) malonic acid (MA) and bromate and (b) H_2SO_4 and ferroin. The inflow concentrations of these reactants to the

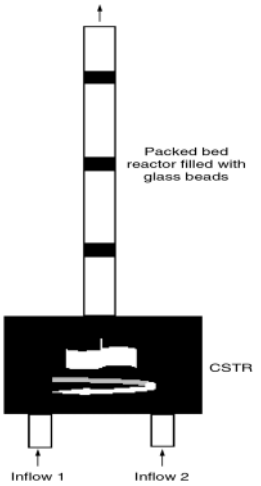

Fig. 1 Schematic diagram of the experimental set-up. Reactants were mixed in the CSTR. The outflow from the CSTR formed the inflow to the PBR.

CSTR were maintained at the following values or ranges: $[MA]_0 = 0.40$ M, $[BrO_3^-]_0 = 0.10$–0.24 M, $[H_2SO_4]_0 = 0.075$–0.20 M and $[ferroin]_0 = 7.0 \times 10^{-4}$ M. The residence time of the CSTR was always such that the system was operated at a stable steady state. The outflow from the CSTR formed the inflow to a packed-bed reactor (PBR) comprised of a vertically-mounted cylindrical glass tube of length 1.5 m and inner diameter 16 mm, packed with spherical glass beads of diameter 3 mm. This packing supports a plug flow along the reactor. The voidage of the PBR was measured to be 33% implying a free cross-sectional area of 0.66 cm^2. A schematic diagram of the experimental set-up is shown in Fig. 1. The development of concentration gradients was recorded by video camera and the resulting images digitised onto a PC for subsequent analysis using the Optimas software package.

3. Experimental results

3.1 Scaling of wavelength with flow velocity and concentrations

An example of a stationary FDO structure obtained in our experiments for a flow velocity $f_P = 0.17$ cm s^{-1}, with $[BrO_3^-]_0 = 0.24$ M, $[H^+] = 0.15$ M and the other reagent concentrations as above is shown in Fig. 2. Ten successive images of the packed-bed reactor are shown from left to right taken at 2 min intervals. The figure, which has been enhanced to highlight the colour change, clearly shows a time-independent, space-periodic structure with oxidised (blue) bands separated by reduced (red) regions. The pattern has a wavelength λ of 15.0 cm. The variation of the wavelength with the flow velocity f_P for a mixture composition with $[BrO_3^-]_0 = 0.20$ M and $[H^+] = 0.15$ M, chosen to match that employed by Kærn and Menzinger, is shown in Fig. 3(a). A linear relationship is confirmed with flow velocities in the range 0.16–0.34 cm s^{-1} yielding wavelengths in the range 18–33 cm. The regression line has a slope of 93.2 ($\pm$5.4) s and an intercept of 2.1 ($\pm$1.4) cm. The gradient compares reasonably well with the natural oscillatory period, $t_P = 130$ s measured for the same composition in a well-stirred batch reactor.

The variation of the wavelength with the inflow concentrations of bromate ion and H^+ has also been examined experimentally for a system with flow velocity $f_P = 0.17$ cm s^{-1}. Both sets of data are plotted in Fig. 3(b) which shows that λ scales linearly with the inverse square root of each concentration. Data points represented by (■) correspond to $[H^+]_0 = 0.15$ M and $[BrO_3^-]_0 = 0.10$–0.24 M; points represented by (●) correspond to $[BrO_3^-]_0 = 0.20$ M and $[H^+]_0 = 0.075$–0.20 M. The linear regression gives a slope of 8.7 ($\pm$0.4) M cm and an intercept of -32.8 ($\pm$2.2) cm. These observations confirm the predicted dependence on the initial concentrations

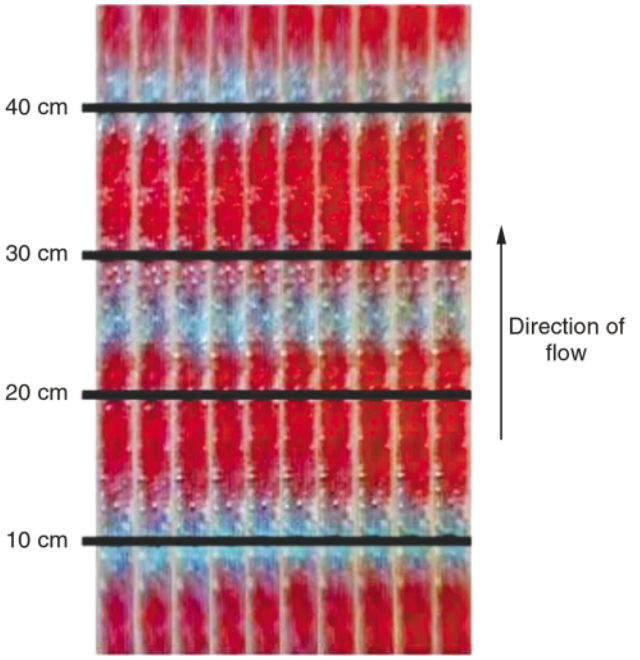

Fig. 2 Experimental images of the FDO pattern in the BZ system for a flow velocity $f_P = 0.17$ cm s^{-1}, with $[BrO_3^-]_0 = 0.24$ M, $[H^+]_0 = 0.15$ M, $[MA] = 0.40$ M and $[ferroin] = 7 \times 10^{-4}$ M. Successive images are taken at 2 min intervals. The wavelength λ is approximately 15 cm.

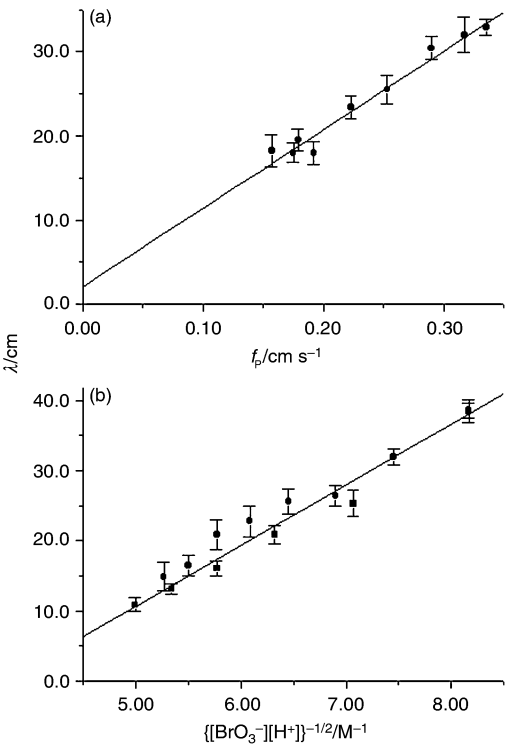

Fig. 3 (a) Experimental dependence of the FDO pattern wavelength on the flow velocity for a system with $[BrO_3^-]_0 = 0.20$ M (other concentrations as in Fig. 2). (b) Experimental dependence of the FDO pattern wavelength on the inflow concentrations of BrO_3^- and H^+ plotted as $\{[BrO_3^-][H^+]\}^{-1/2}$.

derived in our earlier paper based on the Oregonator model. At a given flow velocity, the wavelength is determined as an average over all the bands (typically five) visible in the reactor recorded over a period of 15 min. In some cases, the same flow velocity was repeated in separate experiments. The error bars shown in Fig. 3(a) and (b) represent the scatter of data obtained through this process.

3.2 Dynamics of pattern development

Of particular interest is the initial development of the FDO pattern along the packed-bed reactor as the reagents are introduced to the empty tube. The theoretical interpretations developed previously suggest that the reacting solution will oscillate as it moves up the column, with each fluid element entering the column with the same initial phase and oscillating with a constant fixed period T at some point determined by the constant flow velocity f_P. Thus, we should expect to see the blue bands develop successively, stacking one on top of another starting from the bottom of the tube as the solution fills the reactor.

The observations made in the present study, at least for all the flow velocities employed in the present study, show a markedly different response. The data shown in Fig. 4 indicate the evolution of the first six bands in a system with $f_P = 0.25$ cm s^{-1} with $[BrO_3^-]_0 = 0.20$ M and $[H^+] = 0.15$ M. At a time $\bar{t} = 6.25$ min a *pacemaker* site is seen to develop at a location 35 cm from the bottom of the reactor (note that the fluid column will by this stage have attained a total height of 94 cm, so the pacemaker occurs approximately 40% up the liquid column). This pacemaker yields an oxidation event that splits into two counter-propagating oxidation pulses. One pulse moves up the column with the ascending fluid and weakens in extent (as indicated by the intensity of the blue colour). The other pulse propagates down the reactor, against the fluid flow settling as a stationary band 3 cm wide for $\bar{t} \sim 20$ min, at a position with its lower edge 6 cm above the bottom of the tube. At $\bar{t} = 10.5$ min, a second pacemaker appears at $\bar{x} = 80$ cm and again this leads to two counter-propagating oxidation pulses, the upper of which moves up the column. The lower one again moves down the column and eventually (for $\bar{t} \sim 40$ min) adopts a final position with its lower edge at $\bar{x} = 28$ cm. A third pacemaker also occurs within the field of vision at $\bar{x} = 120$ cm at $\bar{t} = 14.5$ min. The upward-propagating pulse arising from this site rapidly leaves the field of vision: the downward-propagating pulse forming the third FDO band which settles at $\bar{x} = 50$ cm for $\bar{t} \sim 48$ min. Subsequent pacemaker sites occur outside the field of vision, but each produces a pair of oxidation pulses, with the downward propagating pulse entering the field of vision to produce bands 4–6 which settle at $\bar{x} = 76$, 100 and 124 cm respectively. In each case the FDO band has a width of 4 (± 1) cm (the positions quoted refer to the position of the lower edge of these bands). The mechanism for band formation thus involves a "wave splitting" from successive pacemaker sites. Successive pacemaker sites arise at locations separated by *ca.* 40 cm and at a temporal period of *ca.* 240 s.

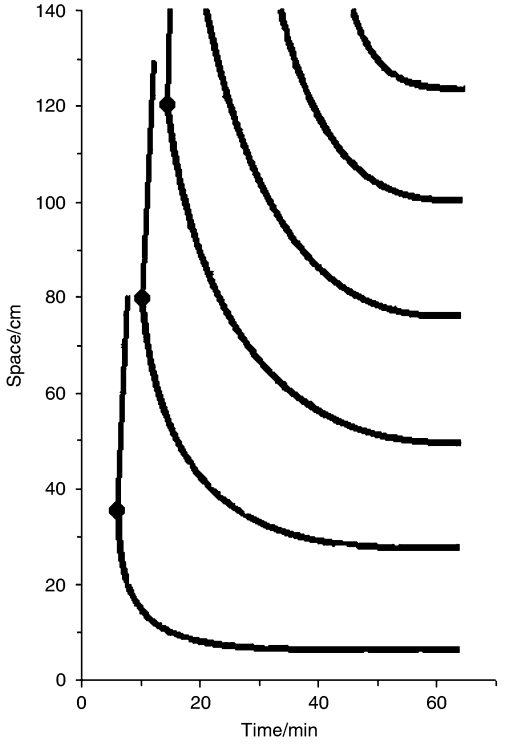

Fig. 4 Experimentally-observed evolution of FDO pattern showing development of pacemaker sites leading to pairs of counter-propagating wave pulses. Circles indicate the first 3 pacemaker sites, all other pacemaker sites occur outside the field of vision. The downward propagating pulses form the FDO pattern bands. Concentrations as in Fig. 3(a).

4. Numerical results

Numerical computations of FDO patterns based on the Oregonator model[8,9] for the BZ system were performed using the methods described in our previous paper. The dimensionless reaction-diffusion-flow equations are taken in the form

$$\frac{\partial u}{\partial t} = \frac{\partial^2 u}{\partial x^2} - \phi_P \frac{\partial u}{\partial x} + \frac{1}{\varepsilon}\left\{u(1-u) - fv\frac{(u-q)}{(u+q)}\right\} \quad (1a)$$

$$\frac{\partial v}{\partial t} = \frac{\partial^2 v}{\partial x^2} - \phi_P \frac{\partial v}{\partial x} + u - v \quad (1b)$$

where u and v represent the dimensionless concentrations of $HBrO_2$ and the oxidised form of the redox catalyst M_{ox} respectively and ϕ_P represents the dimensionless flow velocity. The initial conditions are taken to correspond to the spatially-uniform steady state of these equations subject to a sustained perturbation at $x = 0$ (corresponding to the steady state for a CSTR with dimensionless flow rate $\phi_C = 1$, see ref. 6, section 3) and zero-flux boundary conditions at $x = L$ with typically $L = 200$.

4.1 Scaling of wavelength with flow velocity

The variation of the computed wavelength λ with the flow velocity ϕ_P for three different choices of the parameter ε is shown in Fig. 5 (in each case $f = 1$ and $q = 8 \times 10^{-4}$). For $\varepsilon = 0.8$ and 0.5 the dependence is approximately linear with best-fit gradients of 18.4 (± 0.4) and 12.5 (± 0.1) respectively. The natural oscillatory periods τ_P for these cases are 18.8 and 12.8. For the simple relationship $\lambda = \tau_P \times \phi_P$, the slopes and the oscillatory periods would match. Clearly, there is reasonable agreement in these cases although, as with the experimental observations, there are significant non-zero intercepts. For the case with $\varepsilon = 0.25$, the dependence of the wavelength on the flow velocity is linear at large ϕ_P (with slope 10.5 ± 0.2) but shows significant curvature at low ϕ_P as we approach the minimum flow rate ($\phi_{min} = 1.7$ in this case). This observation of departure from linearity is in agreement with previous computations based on the Rovinsky–Zhabotinsky (ZBKE) model made by Andresen *et al.*[3] It is possible that the non-linearity is more significant for systems with lower ε suggesting that this feature might be detectable in experiments with more excitable systems.

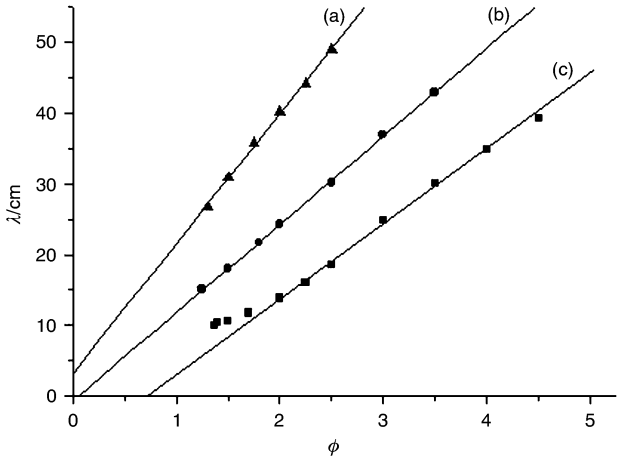

Fig. 5 Numerically-computed dependence of wavelength on flow velocity for Oregonator model with $f = 1$ and $q = 8 \times 10^{-4}$ for different values of ε: (a) $\varepsilon = 0.8$, (b) $\varepsilon = 0.5$, (c) $\varepsilon = 0.25$.

4.2 Development of FDO pattern

The evolution of FDO patterns in a system with $\phi_P = 2.0$, $f = 1$, $\varepsilon = 0.25$ and $q = 8 \times 10^{-4}$ is shown as a space–time plot in Fig. 6. White regions correspond to the reduced redox state (low M_{ox} concentration, red state) and black regions to the oxidised (blue) state. This diagram shows a similar development to that presented from the experimental data in Fig. 4. At various points progressing along the column, at increasing times there is an initiation at a pacemaker site which splits into two wave pulses, one propagating up the reactor with the flow and the other propagating down the reactor to produce a band in the FDO pattern. A total of 14 bands are shown developing in Fig. 6, with the first 11 pacemakers lying within the field of vision. Extensive computations indicate the period between successive pacemaker site development is apparently identical to the natural batch oscillatory period τ_P for the same ε and f and hence the distance between successive pacemaker sites along the column is given by $\phi_P \tau_P$. These computations also indicate that the distance between the uppermost band and the next pacemaker site increases slightly as the number of bands in the pattern increases.

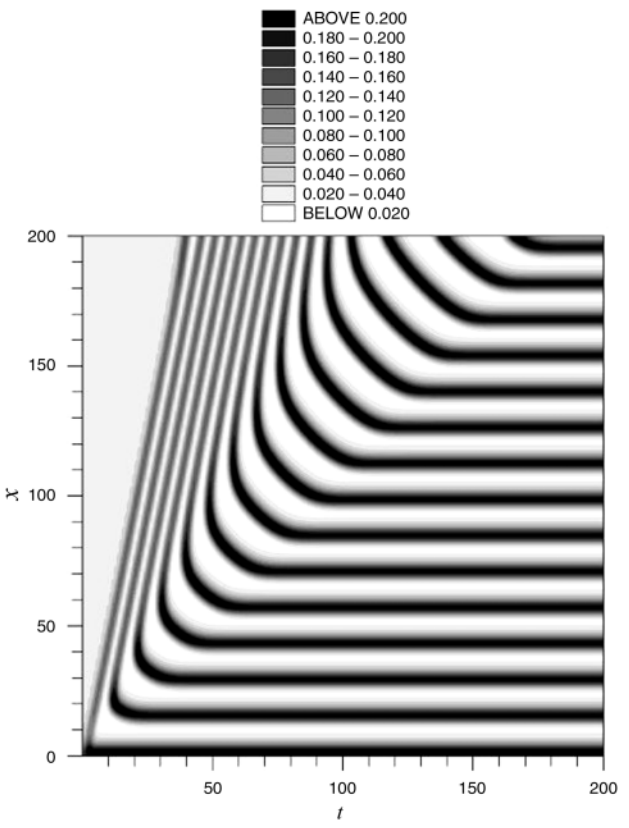

Fig. 6 Space–time plot showing development of FDO patterns for a system with $\varepsilon = 0.25$, $f = 1$ and $\phi_P = 2.0$. The black and white colour code indicates the dimensionless concentration v of the oxidised form of the redox catalyst, with black indicating regions of high oxidation.

The nature of the wave-splitting mechanism is revealed in more detail through the concentration profiles over a sequence of times shown in Fig. 7. Fig. 7(a) corresponds to some arbitrary time zero (actually corresponding to $t = 45$ in Fig. 6) and shows a structure with a boundary layer at $x = 0$, three (stationary) bands of approximately constant amplitude and then a band of somewhat larger amplitude (at $x \sim 60$) which is still propagating downwards. An oxidation pulse is just beginning to develop at $x \sim 95$. Above this there are three full bands corresponding to upward-propagating pulses and a pulse just leaving the top of the diagram. In Fig. 7(b)–(d) the oxidation event at $x \sim 95$ develops fully over approximately 2.4 time units. This pulse then splits into two as the recovery process decreases v, Fig. 7(e). From this develop the next pair of counter-propagating wave pulses, Fig. 7(f), the upper of which propagates with the fluid flow and the lower of which moves towards the FDO bands below, Fig. 7(g). After a period of 9.2 time units, the next pacemaker site is beginning to develop at $x \sim 110$.

4.3 Adjustment of wavelength to changes in flow velocity

The adjustment of an established steady pattern in the reactor following a change (increase) in the flow velocity is shown in the space–time plot in Fig. 8. In this case, there is a relatively simple transition to the new wavelength. The FDO bands all move upwards along the reactor with the new flow, initially keeping their original separation and amplitude. This movement does, however, lead to an increase in the distance separating the first band and the boundary layer which remains fixed at the inlet. As this distance develops, so the amplitude of the first band increases. The first band settles at its new position relative to the inlet and becomes stationary. Now the distance between this band and the second band increases. The amplitude of the second band increases and eventually it attains the appropriate separation from the first band and becomes stationary. This process of increasing separation and amplitude then repeats for the third and subsequent bands until the new stationary pattern is established along the length of the reactor. There is no "wave-splitting" during this "adjustment" process from one established pattern to the next.

4.4 Complex pattern development

For a system with fixed values of f and q, the ε–ϕ_P parameter plane can be divided into several regions by a set of "bifurcation boundaries" determined by the local stability analysis.[2,4,6] The appropriate form of the parameter plane for the present model is shown in Fig. 9, which shows an additional region compared to that reported in Fig. 1 of ref. 6. The "critical" flow velocity $\phi_{P,cr}$ curve given by the solid curve in Fig. 9 is as given in the previous paper and is calculated from the condition

$$\phi_{P,cr} = \sqrt{\frac{4\Delta - Tr^2}{2Tr}} \qquad (1)$$

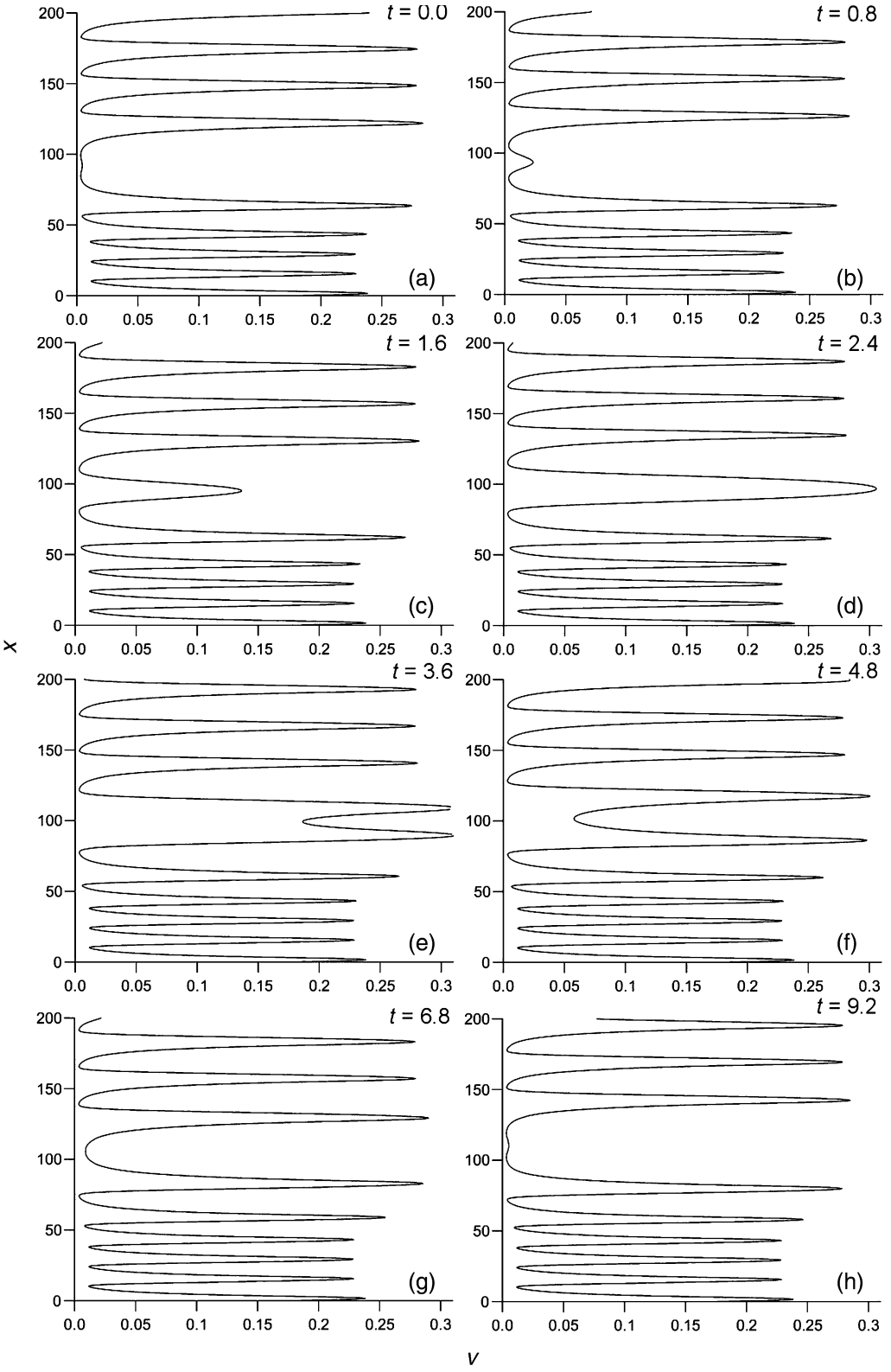

Fig. 7 Instantaneous concentration-profiles for the system in Fig. 6, showing the concentration v along the packed-bed reactor at various times as indicated.

where Tr and Δ are the trace and determinant of the Jacobian matrix for the system (see eqn. (7) in ref. 6). This locus exists over the range $\varepsilon_0 < \varepsilon < \varepsilon_H$ where ε_H is the Hopf bifurcation value corresponding to $\mathrm{Tr} = 0$ and ε_0 corresponds to the condition $4\Delta - \mathrm{Tr}^2 = 0$. With $f = 1$, we have $\varepsilon_0 = 0.490$ and $\varepsilon_H = 0.888$.

Over the same range of ε, there is a second simple curve corresponding to the change from absolute to convective instability, ϕ_{AC}. Over this range, the condition for this bifurcation is given by

$$\phi_{AC} = \sqrt{2\mathrm{Tr}} \qquad (2)$$

as given by eqn. (6) in ref. 6. The critical flow velocity $\phi_{P,cr}$ represents the minimum flow for stationary patterns provided it lies above the absolute-to-convective instability locus, which

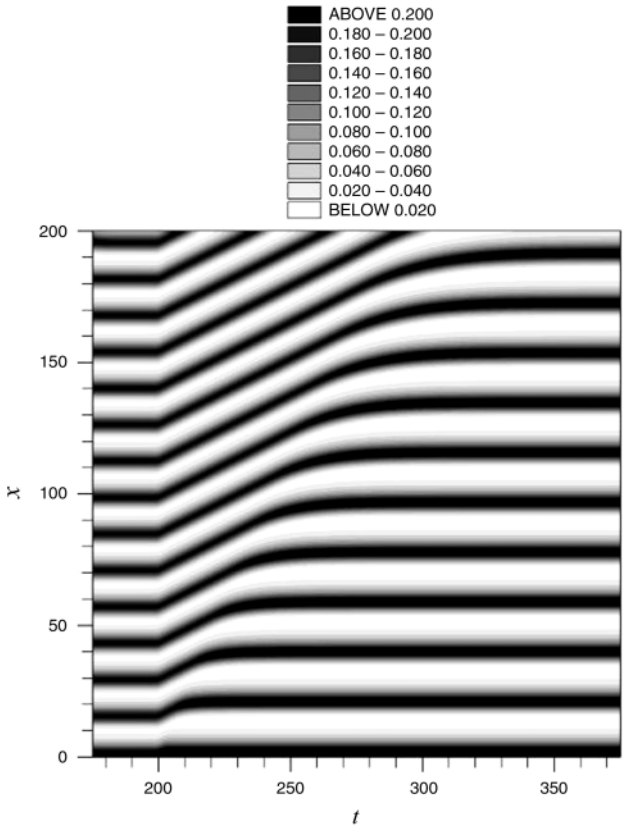

Fig. 8 The adjustment of an FDO pattern to an increase in flow velocity from $\phi_P = 2.0$ to 2.5 applied at $t = 200$. Other parameters as in Fig. 6. Colour scale as in Fig. 6.

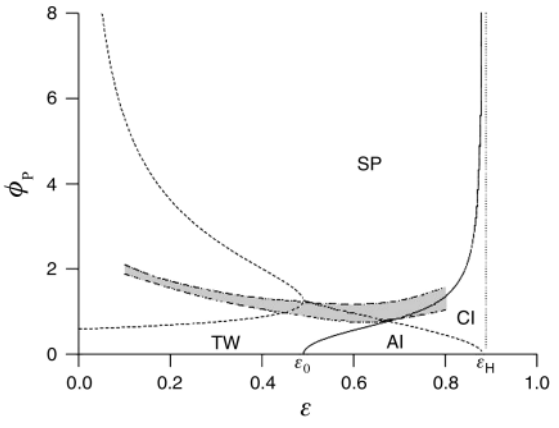

Fig. 9 The bifurcation diagram in the ϕ_P–ε parameter plane showing the boundaries between regions for stationary patterns (SP), transient waves (TW), absolute instability (AI) and convective instability (CI). The shaded region indicates conditions for which complex "resonance patterns" have been observed numerically.

it does for $\varepsilon > ca.\ 0.676$. For lower ε, however, the absolute-to-convective instability locus provides the lower boundary to the region of stationary patterns (SP), separating this response from that of "transient waves" (TW). In the latter mode, the reactor sustains a response in which a pacemaker site at some point along the column periodically initiates a pair of counter-propagating wave-pulses which then propagate towards the two ends of the reactor (see Fig. 3(b) in ref. 6).

For $\varepsilon < \varepsilon_0$, a slightly more careful analysis is required. The bifurcation along the ϕ_{AC} curve corresponds to the imaginary part of the eigenvalue ω governing the temporal evolution of perturbations from the spatially-uniform state passing through zero. For $\varepsilon > \varepsilon_0$, ω is a complex number with non-zero real part and the condition is given by eqn. (2) above. For $\varepsilon < \varepsilon_0$, however, ω is a purely imaginary quantity which we can write as $\omega = i\omega_1$ and $i\omega_2$ given by

$$\omega = \tfrac{1}{2}\{i(\mathrm{Tr} - \tfrac{1}{2}\phi_P^2) \pm \sqrt{4\Delta - \mathrm{Tr}^2}\} \qquad (3)$$

with $4\Delta - \mathrm{Tr}^2$ being negative for $\varepsilon < \varepsilon_0$ so the whole right-hand side is imaginary. (For further details see ref. 4, section 3(a), eqn. (21).) The bifurcation locus in Fig. 9 now splits into two, one corresponding to ϕ_P such that $\omega_1 = 0$ and the other to ϕ_P such that $\omega_2 = 0$. Along the lower branch, $\omega_1 = 0$, say. Below this branch, ω_1 and ω_2 are both positive so the system is temporally unstable. For flow rates lying between the two branches of the bifurcation locus, the roots are such that $\omega_1 < 0$ and $\omega_2 > 0$. The system is still temporally unstable as the term associated with the second eigenvalue grows in time, although there is now a saddle point character. For higher flow-rates, above the upper branch (along which $\omega_2 = 0$), both ω_1 and ω_2 are negative. The stationary pattern is now temporally stable.

We have examined the initial development of the FDO patterns for a variety of flow rates and ε values with particular attention to systems lying close to the various bifurcation boundaries associated with transient wave solutions (TW) and stationary patterns (SP).

The space–time plots for systems with $\varepsilon = 0.25$ and with flow velocities $\phi_P = 1.5$ and 1.4 are shown in Fig. 10(a) and (b) respectively. For the former, following the initial wave disturbing the system from its initial steady state, we see the development of successive pacemaker sites along the reactor leading to the development of counter-propagating pulses as described previously. The upward-propagating pulse leaves the reactor, and the downward-propagating pulse approaches the existing FDO pattern. In the previous case described with $\phi_P = 2.0$ (Fig. 6), each downward-propagating pulse settled to form a new band in the pattern. For this lower flow velocity, however, a more complex situation evolves. The first three bands after the boundary layer are established as before, but as the next pulse (the fourth) approaches it fails to establish the next band and the pulse collapses (at $x \sim 40$, $t \sim 50$). Significantly, there is a small "bulge" in the third band as the fourth pulse approaches. The fifth pulse is able to settle to provide the fourth band in the pattern ($x \sim 42$, $t \sim 60$). The sixth pulse again fails as it approaches the FDO pattern ($x \sim 51$ and $t \sim 78$) but the seventh does set up the fifth band ($x \sim 54$, $t \sim 90$). This simple pattern of alternation between band formation and decay continues for one more cycle and can also be seen later in the space–time plot (over the range $90 < x < 150$). In between these "laminar" phases and at later times, there is a slightly more complex story with sometimes two wave pulses failing before the next band is established or bands being formed from successive pulses.

This complexity is further developed for the case with $\phi_P = 1.4$, which is closer to the boundary. As shown in Fig. 10(b), band formation does occur to yield a very regular stationary pattern, but in between each band formation step, several wave pulse can arrive and fail. In each case of wave pulse failure, the preceding band can be seen to show a "bulge" in the space–time plot as the pulse approaches. Examination of the concentration profiles for these cases indicates that the amplitude of any given band varies considerably through a damped oscillatory approach to its final value—*i.e.* there is distinct *focal* character to the pattern for these operating conditions. If a wave pulse approaches a band that is entering a phase with a high extent of oxidation—and consequently of inhibitor production—then it appears that it is likely to be quenched and hence unable to establish a new

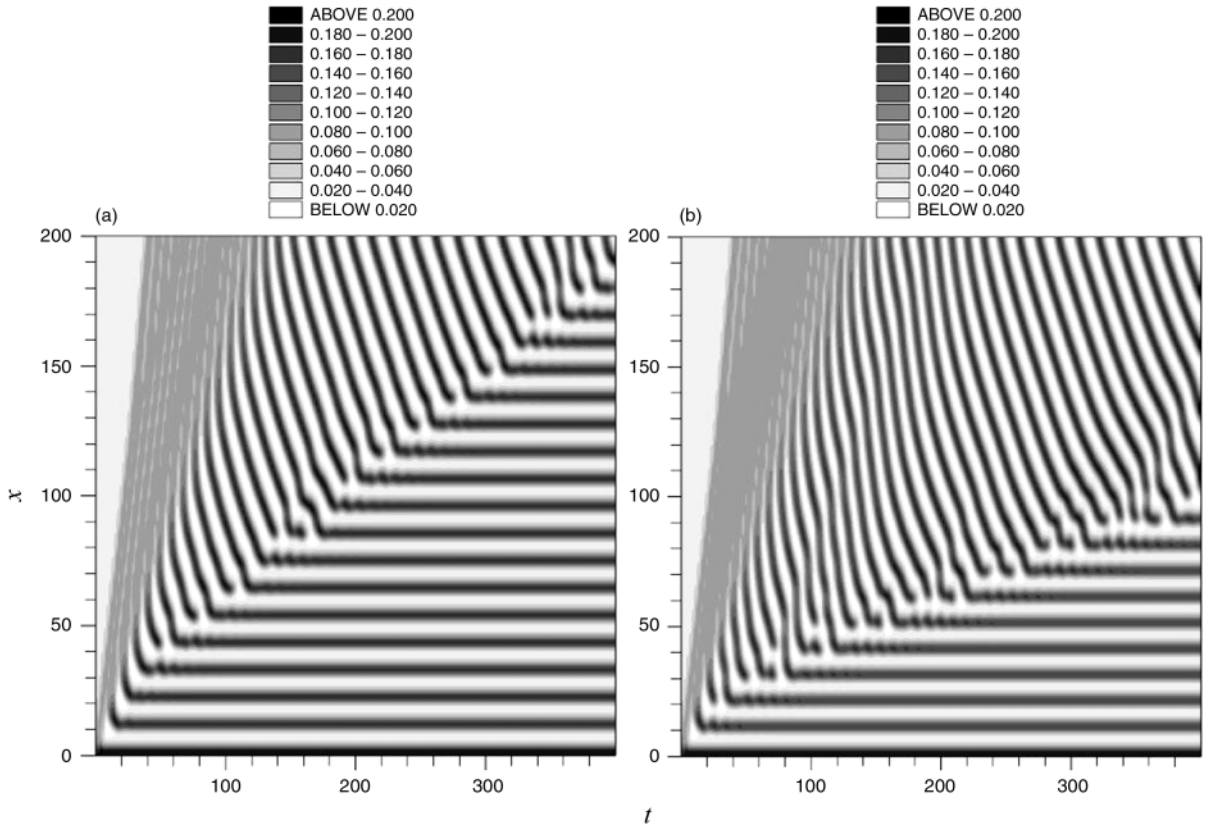

Fig. 10 Space–time plots showing complex "resonance pattern" evolution: $\varepsilon = 0.25$, $f = 1$ with (a) $\phi_P = 1.5$ and (b) $\phi_P = 1.4$. Colour scale as in Fig. 6.

band (the width of the existing band increases slightly as it undergoes this "overshoot" of its steady-state amplitude, so the distance between this and the approaching pulse then is less than the stationary-state wavelength). As subsequent wave pulses approach, the band may be approaching its final amplitude and any overshoots are of sufficiently small extent to allow the next band to be established.

The parameter combinations for which such complex transient dynamics were observed in our computations are indicated as the shaded region on Fig. 9.

5. Discussion and conclusions

The experimental and numerical results presented above confirm some aspects of the "simple view" of "flow distributed oscillations" but also reveal new and hitherto unexpected features. The "simple view" that the patterns are simply phase waves spread along the packed bed reactor by the flow is consistent with the reasonable agreement between the period estimated from the dependence of the pattern wavelength on the flow velocity revealed in Fig. 3 and 5. In these plots, the data are taken from the long-time steady structures observed. However, the dynamic evolution through which these patterns evolve is more complex than expected. The interpretation of distance along the reactor being representative of a reaction time cannot be maintained when considering the wave-splitting that leads to pulses propagating against the flow, *i.e.* "backwards in time". Such a feature occurs most notably at low flow velocities where the diffusional spreading from the pacemaker in both directions can most easily compete with the unidirectional convective flow. However, such is the nonlinear amplification of diffusion by the nonlinear chemistry of this excitable system that even at relatively high flow rates, the wave-splitting mechanism continues to operate (at least for systems with $f = 1$).

For flow velocities close to the transition from stationary patterns to transient waves, complex dynamics are observed. This feature appears to have some similarity to the "resonance patterns" described by Tóth *et al.*[10] who studied the transmission of BZ waves through capillary tubes. In those experiments, waves of excitability were generated on one side of a capillary channel. The waves propagated along the channel and could emerge into a fresh excitable medium. If the diameter of the channel is sufficiently high, the emerging wave initiates a wave in this second compartment. If the channel diameter is too small (below the "critical diameter"), then no wave initiation occurs. For a range of diameters close to but above the critical diameter, the response depends on the period of the waves entering the tube and is characterised by a *firing number*, $1/n$ such that $n = 1, 2$ *etc.* is the number of waves entering the tube for every successful initiation. Tóth *et al.*[10] established that the firing numbers correspond to a branch of a Farey tree. It is possible that such a structure also arises in the present system—so, for instance, the majority of the response in Fig. 10(a) would correspond to a firing number of 1/2, with one band created for every two downward propagating pulses. The complexity again increases as we approach a "criticality"—in this case the bifurcation from absolute to convective instability. It is likely that a deeper understanding of the onset of this complexity can be traced to the phase-plane trajectory of the local evolution for the reaction–transport system in a similar way to that presented in ref. 10 in which it was shown that diffusional loss through curvature allowed the trajectory to be deflected back across the nullcline branch that forms excitation threshold. This point will be considered further elsewhere.

Acknowledgements

This work was supported by the British Council and the Hungarian Scholarship Board (Ministry of Education) under the Joint Academic Research Programme (project no. 010), by the ESF Scientific Programme REACTOR and by the Hungarian Research Grants OTKA T025375 and FKFP 0455/1997.

References

1 S. P. Kuznetsov, E. Mosekilde, G. Dewel and P. Borckmans, *J. Chem. Phys.*, 1997, **106**, 7609.
2 P. Andresen, M. Bache, E. Mosekilde, G. Dewel and P. Borckmanns, *Phys. Rev. E*, 1999, **60**, 297.
3 P. Andresen, E. Mosekilde, G. Dewel and P. Borckmans, *Phys. Rev. E*, 2000, **62**, 2992.
4 J. R. Bamforth, S. Kalliadasis, J. H. Merkin and S. K. Scott, *Phys. Chem. Chem. Phys.*, 2000, **2**, 4013.
5 M. Kærn and M. Menzinger, *Phys. Rev. E*, 1999, **60**, R3471.
6 J. R. Bamforth, J. H. Merkin, S. K. Scott, R. Tóth and V. Gáspár, *Phys. Chem. Chem. Phys.*, 2001, **3**, 1435.
7 A. A. Schilt, *Analytical applications of 1,10-phenanthroline and related compounds*, Pergamon, Oxford, 1969.
8 R. J. Field and R. M. Noyes, *J. Chem. Phys.*, 1974, **60**, 1877.
9 J. J. Tyson and P. C. Fife, *J. Chem. Phys.*, 1980, **73**, 2224.
10 Á. Tóth, V. Gáspár and K. Showalter, *J. Phys. Chem.*, 1994, **98**, 522.